A Reverse Shock in GRB 130427A

A Reverse Shock in GRB 130427A

T. Laskar[1], E. Berger[1], B. A. Zauderer[1], R. Margutti[1], A. M. Soderberg[1], S. Chakraborti[1], R. Lunnan[1], R. Chornock[1], P. Chandra[2], and A. Ray[2]

Received _____; accepted _____

[1]Harvard-Smithsonian Center for Astrophysics, 60 Garden Street, Cambridge, MA 02138

[2]Tata Institute of Fundamental Research, Homi Bhabha Road, Mumbai 400 005, India

ABSTRACT

We present extensive radio and millimeter observations of the unusually bright GRB 130427A at $z = 0.340$, spanning 0.67 to 12 d after the burst. Taken in conjunction with detailed multi-band UV, optical, NIR, and X-ray observations we find that the broad-band afterglow emission is composed of distinct reverse shock and forward shock contributions. The reverse shock emission dominates in the radio/millimeter and at $\lesssim 0.1$ d in the UV/optical/NIR, while the forward shock emission dominates in the X-rays and at $\gtrsim 0.1$ d in the UV/optical/NIR. We further find that the optical and X-ray data require a Wind circumburst environment, pointing to a massive star progenitor. Using the combined forward and reverse shock emission we find that the parameters of the burst are an isotropic kinetic energy of $E_{\rm K,iso} \approx 2 \times 10^{53}$ erg, a mass loss rate of $\dot{M} \approx 3 \times 10^{-8}$ M$_\odot$ yr^{-1} (for a wind velocity of $1,000$ km s^{-1}), and a Lorentz factor at the deceleration time of $\Gamma(200\,{\rm s}) \approx 130$. Due to the low density and large isotropic energy, the absence of a jet break to ≈ 15 d places only a weak constraint on the opening angle, $\theta_j \gtrsim 2.5^\circ$, and therefore a total energy of $E_\gamma + E_K \gtrsim 1.2 \times 10^{51}$ erg, similar to other GRBs. The reverse shock emission is detectable in this burst due to the low circumburst density, which leads to a slow cooling shock. We speculate that this is a required property for the detectability of reverse shocks in the radio and millimeter bands. Following on GRB 130427A as a benchmark event, observations of future GRBs with the exquisite sensitivity of VLA and ALMA, coupled with detailed modeling of the reverse and forward shock contributions will test this hypothesis.

1. Introduction

Although long-duration γ-ray bursts (GRBs) have been associated with the deaths of massive stars (Woosley & Bloom 2006), the precise nature of their progenitors, the structure of their explosion environments, and the composition of their ejecta remain only partially explored. Studies of the afterglow (forward shock) emission provide insight on the explosion energy, geometry, and the structure of the circumburst medium (e.g., Sari et al. 1998; Chevalier & Li 2000). On the other hand, the most useful probe of the initial bulk Lorentz factor and the ejecta composition is afforded by the reverse shock, which is expected to produce a similar synchrotron spectrum as the forward shock, with well-defined properties relative to the forward shock (e.g., Sari & Piran 1999b; Kobayashi & Zhang 2003a; Zou et al. 2005).

The expected observational signature of the reverse shock is early time flares in the optical and radio bands, and several studies have found hints of excess early-time emission attributable to a reverse-shock like component (e.g. Akerlof et al. 1999; Sari & Piran 1999a; Kulkarni et al. 1999; Soderberg & Ramirez-Ruiz 2002; Kobayashi & Zhang 2003b; Berger et al. 2003; Soderberg & Ramirez-Ruiz 2003; Chevalier et al. 2004). However, a detailed understanding of the reverse shock emission requires a careful decomposition of the afterglow spectral energy distribution into the reverse and forward shock components. Since the peak frequencies of the two components are related by a factor of $\Gamma^2 \gtrsim 10^4$, such a decomposition requires multi-wavelength observations spanning several orders of magnitude in frequency. Similarly, the density profile of the environment affects the hydrodynamic evolution of both the forward and reverse shocks, leading to discernible differences in the behavior of light curves. Consequently, well-sampled light curves are also essential for any systematic study of reverse shocks.

Such data sets have not been available to date primarily due to sensitivity limitations of radio and millimeter facilities. However, the recent upgrade of the VLA to the Karl G. Jansky Very Large Array (JVLA), with an order of magnitude improvement in sensitivity has opened

a new avenue for the study of reverse shocks in GRBs. Here we present the first example of a reverse shock detected in a multi-wavelength data set spanning 1–100 GHz of the nearby energetic GRB 130427A. By combining our detailed radio and millimeter observations with X-ray data from *Swift* and UV/optical/NIR observations from *Swift* and ground-based telescopes, we present the most comprehensive data set for reverse shock studies to date. We undertake a joint model fit to the entire data set and extract parameters for the explosion and the environment, and draw general conclusions on reverse shock studies in the JVLA and ALMA era.

2. Observations and Data Analysis

2.1. GRB Discovery

GRB 130427A was discovered by the *Swift* (Gehrels et al. 2004) Burst Alert Telescope (BAT, Barthelmy et al. 2005) on 2013 April 27 at 07:17:57 UT (Maselli et al. 2013) with a duration of $T_{90} = 163$ s and a fluence of $F_\gamma = 3.1 \times 10^{-4}$ erg cm^{-2} (15–150 keV; Barthelmy et al. 2013). The burst was also detected with the *Fermi* Gamma-ray Burst Monitor (GBM; Meegan et al. 2009), 50.6 s before the *Swift* trigger[1] with an unusually large fluence of $F_\gamma = 2 \times 10^{-3}$ erg cm^{-2} (10–1000 keV) and a peak energy of $E_{\rm p} = 830$ keV (von Kienlin 2013). Coincident high-energy γ-ray emission was detected by the *Fermi* Large Area Telescope (LAT; Atwood et al. 2009) up to 94 GeV (Zhu et al. 2013).

The *Swift* X-ray Telescope (XRT, Burrows et al. 2005) began observing the field 140 s after the BAT trigger, leading to the detection of the X-ray afterglow, localized to RA(J2000) = 11$^{\rm h}$ 32$^{\rm m}$ 32.63$^{\rm s}$, Dec(J2000) = +27° 41 ’ 51.7 ", with an uncertainty radius of 3.5 arcseconds (90% containment, Kennea et al. 2013). The *Swift* UV/Optical Telescope (UVOT, Roming et al. 2005)

[1]In our analysis, we take the GBM trigger time as the start time of the event, t_0

began observing the field 150 s after the burst, leading to the detection of a bright UV/optical afterglow (Maselli et al. 2013), which was subsequently detected by several ground-based observatories in the optical (e.g. Elenin et al. 2013; Perley 2013b; Melandri et al. 2013; Morgan 2013; Yatsu et al. 2013), NIR (Morgan 2013), millimeter (Zauderer et al. 2013b; Perley 2013a), and radio (Zauderer et al. 2013a; Volvach et al. 2013; Corsi 2013). Spectra were obtained at *Gemini*-North, the *Nordic Optical Telescope*, and the *VLT* resulting in a redshift of $z = 0.340$ (Levan et al. 2013; Xu et al. 2013; Flores et al. 2013), and leading to an isotropic equivalent γ-ray energy of $(1.05 \pm 0.15) \times 10^{54}$ erg ($E_{\gamma,\rm iso}$ = 1–10^4 keV, rest frame; Amati et al. 2013).

2.2. Radio to X-ray Observations

We observed the position of GRB 130427A beginning on 2013 April 27.99 UT (Δt = 0.67 d) with the Karl G. Jansky Very Large Array (VLA) at a mean frequency of 5.8, GHz and with the Combined Array for Research in Millimeter Astronomy (CARMA; Bock et al. 2006) beginning on 2013 April 28.13 UT (Δt = 0.81 d) at a mean frequency of 85 GHz. In both observations, we detect a strong radio source coincident with the optical afterglow position. The data were obtained in the standard continuum modes utilizing the VLA's WIDAR correlator (Perley et al. 2011) with a total bandwidth of $\sim$2 GHz, and CARMA's continuum mode with a bandwidth of $\sim$8 GHz. For VLA observations we utilized 3C286 for bandpass and flux calibration, and J1125+2610 for gain calibration in all but one epoch, where J1159+2914 was utilized as the gain calibrator for observing frequencies greater than 15 GHz. For all CARMA observations we utilized 3C273 for primary flux calibration and 0854+201 for bandpass calibration. For gain calibration, we utilized 1224+213, and a source-gain cycle of $\sim$15 min. We analyzed the VLA observations using the Common Astronomy Software Applications (CASA; McMullin et al. 2007) and the Astronomical Image Processing System (AIPS; Greisen 2003), and the CARMA observations using the Multi-channel Image Reconstruction, Image Analysis, and Display software (MIRIAD;

Sault et al. 1995). In all cases, we flagged edge channels and any data corrupted with radio frequency interference. We measured the flux density of the afterglow in the final images using the AIPS task JMFIT. We also observed GRB 130427A with the Giant Metrewave Radio Telescope (GMRT) at central frequencies of 1390 MHz and 610 MHz (bandwidth of 32 MHz), using 3C 147 and 3C 286 as flux and bandpass calibrators, and J1125+261 and J1227+365 as phase calibrators. We analyzed the data using AIPS. A summary of all radio and millimeter observations is provided in Table 1.

We extracted *Swift*/XRT spectra at the times of our radio observations (at 58, 173, 406, and 786 ks) using the latest version of the HEASOFT package (v. 6.13) and corresponding calibration files, following standard procedures (Evans et al. 2007, 2009; Margutti et al. 2013). The spectra are well fit by an absorbed single power-law model with $N_{\rm H,Gal} = 1.80 \times 10^{20}$ cm^{-2} (Kalberla et al. 2005), intrinsic hydrogen column $N_{\rm H,int} = (6.64 \pm 0.01) \times 10^{20}$ cm^{-2} and photon index $\Gamma = 1.76 \pm 0.03$ (68% confidence intervals). We find no statistically significant evidence for spectral evolution. We obtain XRT light curves by converting the 0.3–10 keV count rates reported on the *Swift* website[2] to a flux density at 1 keV using the measured spectral model (Evans et al. 2007, 2009).

Swift/UVOT observed GRB 130427A using 6 filters spanning the central wavelength range $\lambda_c = 1928$ Å (*w2*) to $\lambda_c = 5468$ Å(*v*). We analyzed the UVOT data using the latest version of HEASOFT (v. 6.13) and corresponding calibration files with a 5″ aperture extract on in the UVOT photometric system (Breeveld et al. 2011). The *Swift* star trackers failed to find a correct aspect solution during the first 1.9 ks of exposure. For these data, we manually checked each frame and corrected the position of the extraction region to account for the drifting of the source . The source point spread function appears to be highly distorted in the first two frames acquired in *v*-band, while the first frames in the *b* and *u* bands suffer from significant coincidence losses due to the

[2] http://www.swift.ac.uk/xrt_curves/00554620/

brightness of the afterglow. We do not use these exposures in our analysis.

We also obtained three epochs of $g'r'i'$ photometry of the optical afterglow using the MMTcam imager on the MMT 6.5m telescope[3]. A sequence of 2×150 s dithered images in each band was taken on 2013 May 2.43 UT, of 2×250 s (in g' and r') and 2×300 s (in i') on 2013 May 4.43 UT, and 3×300s in each band on 2013 May 8.44 UT. The images were bias-and dark-subtracted, flat-fielded and stacked using standard routines in IRAF[4]. The combined flux of the GRB and host galaxy was measured using aperture photometry with an aperture size of 2.5 times the seeing of the images, and calibrated relative to the SDSS photometry of the nearby star SDSSJ113231.32+274222.7.

Finally, we collected all publicly-available photometry from the GCN Circulars and converted the reported magnitudes to flux densities at the following central wavelengths: g' : 445 nm, V : 551 nm, R : 658 nm, I : 806 nm, z' : 900 nm, Y : 1020 nm, J : 1220 nm, H : 1630 nm, and K : 2190 nm. For magnitudes reported in the Vega system, we used the zero-points from Bessell et al. (1998).

3. Basic Considerations

We interpret the observed behavior of the afterglow emission from radio to X-rays in the framework of the standard synchrotron model, described by three break frequencies (self-absorption: ν_a; characteristic synchrotron frequency: ν_m; and synchrotron cooling: ν_c), and an overall flux normalization. In this model, there are well-defined relations between the

[3]http://www.cfa.harvard.edu/mmti/wfs.html

[4]IRAF is distributed by the National Optical Astronomy Observatories, which are operated by the Association of Universities for Research in Astronomy, Inc., under cooperative agreement with the National Science Foundation.

temporal evolution and spectral indices that allow us to determine the location of the synchrotron frequencies as well as the density profile of the circumburst medium (ISM profile: ρ = const; Wind: $\rho \propto r^{-2}$). The models are described in detail in Sari et al. (1998) and Chevalier & Li (2000).

A striking feature of the afterglow light curves is the unbroken power-law decline in the X-rays with $\alpha_X \approx -1.35$ at $\gtrsim 200$ s ($F_\nu \propto t^\alpha$). Given the X-ray spectral index of $\beta_X \approx -0.76$ during this time ($F_\nu \propto \nu^\beta$), we expect an X-ray decline rate of $\alpha_X = -0.64$ if $\nu_c < \nu_X$ (independent of the circumburst density profile), while for $\nu_c > \nu_X$, we expect $\alpha_{\rm X} \approx -1.14$ for an ISM profile or $\alpha_{\rm X} \approx -1.64$ for a Wind profile. Since the decline rate predicted in the ISM model is always shallower than the observed value, we conclude that a Wind profile is required, with $\nu_c \sim \nu_X$ providing a reasonable match to the observed decline. This conclusion is further supported by the similar decline rate in the UV/optical/NIR band at $\gtrsim 0.3$ d, $\alpha_{\rm opt} \approx -1.35$, which indicates that the optical and X-ray bands are located on the same portion of the synchrotron spectrum (i.e., $\nu_m < \nu_{\rm opt} < \nu_X \sim \nu_c$). Indeed, as shown with the broad-band spectral energy distributions in Figure 1, the NIR/X-ray spectral index at ≈ 2.0 d is $\beta_{\rm NIR,X} \approx -0.70$ in agreement with our conclusion that the optical and X-ray bands are located on the same synchrotron slope. On the other hand, the spectral index within the UV/optical/NIR bands, $\beta_{\rm opt} \approx -0.85$, is steeper, indicating that modest extinction is present. The observed optical and X-ray decline rates require an electron power law index of $p \approx 2.2$, in good agreement with the observed spectral index. We note that in the Wind model $\nu_{\rm c} \propto t^{1/2}$ and hence once it crosses the X-ray band, the X-ray flux is expected to decline as an unbroken power law, matching the observed behavior.

Whereas the X-ray light curve follows a single power law decline, the UV/optical/NIR light curves display a clear change in slope at ≈ 0.1 d (see Figure 2). The initial slope is shallower, with $\alpha_{\rm opt} \approx -0.8$, and the time of the break is chromatic, occurring later in the redder filters. In the Wind model, the passage of ν_m through an observing band results in a transition from $\alpha = 0$ to $\alpha = (1-3p)/4 \approx -1.4$ (for $p = 2.2$) in clear contrast to the observed evolution. This indicates that

a different emission component dominates the UV/optical/NIR light curves at $\lesssim 0.1$ d.

Even stronger evidence for a distinct emission component is provided by the radio and millimeter data. The relatively flat spectral index between the radio/millimeter and optical bands at all times, $\beta_{\rm radio,opt} \approx -0.25$, is inconsistent with a single power-law extrapolation from the optical. This shallow slope cannot be caused by the location of ν_m between the radio and optical bands because all light curves below ν_m should be flat in the Wind model, while the observed radio and millimeter light curves clearly decline at all frequencies spanning 6.8 to 90 GHz. Similarly, the expected spectral index below ν_m is $\beta = 1/3$ or 2 (the latter if ν_a is located above an observing band), while we observe instead $\beta_{\rm radio} \approx -0.2$ at $\Delta t \approx 2$–5 d (Figure 1).

One possibility to flatten the spectral slope between the radio and optical bands is to introduce a break in the electron energy distribution at $\gamma_{\rm b}$ such that $N(\gamma) \propto \gamma^{-p_2}$ (with $p_2 < 2$) for $\gamma_{\rm m} < \gamma < \gamma_{\rm b}$. For the observed value of $\beta_{\rm radio,opt}$ this requires $p_2 \approx 1.4$. However, for this lower value of p we expect a shallower decline rate in the radio and millimeter of $\alpha \approx -0.8$, while the observed decline in the millimeter bands is $\alpha_{\rm mm} \approx -1.5$. This argues against a break in the electron spectrum as the cause for the shallow radio/optical spectral slope.

Instead, the distinct spectral and temporal behavior in the radio and millimeter clearly requires a different synchrotron emission component, which is also required to explain the UV/optical/NIR data at $\lesssim 0.1$ d. We associate this component with the reverse shock, and show in detail in the next section that it can explain the radio and millimeter data, as well as the early optical data. To gain insight into the reverse shock spectrum we note that the SED at 0.67 d (Figure 1) requires $\nu_{\rm m}$ to be located between 10 and 90 GHz, with an optically-thin spectrum extending to the optical. In addition, the spectral index between 5.1 and 6.8 GHz, $\beta \approx 1.8$, is indicative of self-absorption, with $\nu_{\rm a} \approx 7$ GHz. The optically thin spectrum observed in the radio at about 2.0 d indicates that $\nu_a \lesssim 5$ GHz at that time. Additionally, since the emission from a reverse shock cuts off exponentially above ν_c, whereas we invoke some contribution from this

component to the UV flux at $\lesssim 0.1$ d, we require $\nu_c \gtrsim 10^{15}$ Hz for the reverse shock at ≈ 0.1 d.

To summarize, the optical data at $\gtrsim 0.1$ d, when combined with the full X-ray light curve at $\gtrsim 200$ s, require a Wind medium with $p \approx 2.2$, $\nu_c \sim \nu_X$, and $\nu_m \sim \nu_{opt}$ at ~ 0.1 d. In addition, the radio and millimeter emission and the early optical emission at $\lesssim 0.1$ d cannot be accommodated with the same synchrotron spectrum, and therefore require a separate emission component. This emission component has $\nu_a \approx 7$ GHz and $\nu_m \approx 10-90$ GHz at 0.67 d, as well as $\nu_c \approx 10^{15}$ Hz at 0.1 d. In the next section we expand on these results with full broad-band modeling of the forward and reverse shock emission.

4. A Self-consistent Reverse Shock/Forward Shock Model

Based on the basic considerations described in the previous section, we construct a model SED for the radio to X-ray emission at 0.67 d (Figure 1). The model is composed of two emission components: (1) a forward shock (FS) which peaks between the millimeter and optical bands, fits the NIR to X-ray SED, and provides negligible contribution in the radio/millimeter; and (2) a reverse shock (RS) which fits the radio to millimeter SED, and provides negligible contribution at higher frequencies. The synchrotron parameters of the reverse shock are $\nu_{a,RS} \approx 7$ GHz, $\nu_{m,RS} \approx 20$ GHz, $\nu_{c,RS} \approx 10^{13}$ Hz, and $F_{\nu m,RS} \approx 10$ mJy. The synchrotron parameters describing the forward shock are $\nu_{a,FS} < 5$ GHz, $\nu_{m,FS} \approx 4 \times 10^{13}$ Hz, $\nu_{c,FS} \approx 2 \times 10^{17}$ Hz, and $F_{\nu,m,FS} \approx 3$ mJy. Both SEDs are in the slow cooling regime with the standard ordering of the synchrotron break frequencies, $\nu_a < \nu_m < \nu_c$. We find that this combined RS plus FS model with a common value of $p \approx 2.2$ completely describes the observed SED at 0.67 d (Figure 1).

We evolve both emission components in time to the other three epochs where we have extracted multi-wavelength SEDs. The evolution of the RS spectrum depends upon whether the shock is relativistic or Newtonian in the frame of the unshocked ejecta. Zou et al. (2005) derive

the temporal evolution of the RS break frequencies, both before and after the ejecta crossing time (the so-called deceleration time, $t_{\rm dec}$) in the two asymptotic regimes of relativistic and Newtonian evolution. An important constraint on the shock evolution is provided by an *R*-band flux density of about 77 mJy measured by the Faulkes Telescope North at ≈ 4.3 min (Melandri et al. 2013). We find that a relativistic RS over-predicts this early optical emission by about a factor of five. In addition, in the relativistic case both $\nu_{\rm m,RS}$ and $\nu_{\rm c,RS}$ evolve as $t^{-15/8}$, leading to a predicted decline rate of $t^{-3(5p+1)/16} \sim t^{-2.25}$ above $\nu_{\rm m,RS}$ (for $p = 2.2$), which is significantly steeper than the observed decline rate, $\alpha_{\rm mm} \approx -1.5$. The Newtonian RS model, on the other hand, offers an additional degree of freedom via the profile of the shocked ejecta, $\gamma \propto r^{-g}$, where we expect $1/2 < g < 3/2$ from theoretical considerations (Zou et al. 2005), although a value of $g > 3/2$ was found for GRB 990123 (Soderberg & Ramirez-Ruiz 2003). We treat g as a free parameter and find a good match to the SED evolution with $g \approx 5$. In the following, we focus on the Newtonian RS case.

Our implementation of the FS follows the smoothly-connected power-law synchrotron spectrum for the Wind environment of Granot & Sari (2002), where we compute the break frequencies and normalizations using the standard microphysical parameters (ϵ_e and ϵ_B), the explosion energy ($E_{\rm K,iso}$), and the circumburst density in the Wind profile (A_*). We also use the SMC extinction curve (Pei 1992) to model the extinction in the host galaxy ($A_{\rm V}$). We use the flux density of the host galaxy in the *griz* filters as measured in the Sloan Digital Sky Survey as an additive component to the relevant filters. Having determined a set of values for the break frequencies of the RS spectrum at 0.67 d, we evolve these parameters based on the Newtonian evolution, and fit separately for the FS contribution to the total flux at all frequencies. We determine the FS parameters using all of the available photometry simultaneously with a combination of RS and FS spectra. To efficiently and rapidly sample the available parameter space, we carry out a Markov Chain Monte Carlo (MCMC) analysis using a python implementation of the ensemble MCMC sampler EMCEE (Foreman-Mackey et al. 2012).

We find that the self-absorption frequency of the forward shock ($\nu_{\rm a,FS}$) declines below about 300 MHz at 0.5 hr after the burst and is not directly observed thereafter. Consequently, the derived blastwave parameters are degenerate with respect to $\nu_{\rm a,FS}$; we quote all results in terms of this frequency, scaled to 14 MHz at 1 day (Table 2). Imposing the theoretical restrictions $\epsilon_e, \epsilon_B \leq 1/3$ we further constrain the blastwave parameters to the following narrow ranges: $12\,{\rm MHz} < \nu_{\rm a,FS} < 16\,{\rm MHz}$, $0.25 < \epsilon_e < 0.33$, $0.14 < \epsilon_B < 0.33$, $2.1 \times 10^{-3} < A_* < 3.7 \times 10^{-3}$, and $4.4 < E_{\rm K,iso,52} < 5.8$. Marginalizing the posterior density functions, we find the following median values of the forward shock parameters: $p = 2.23$, $\epsilon_{\rm e} = 0.30$, $\epsilon_B = 0.20$, $A_* = 2.9 \times 10^{-3}$, $E_{\rm K,iso,52} = 4.9$, and $A_{\rm V} = 0.18$ mag. The FS spectrum transitions from fast cooling to slow cooling around $\Delta t \approx 1200$s. The best-fit combined RS and FS model is shown for the multi-epoch SEDs in Figure 1 and for all available radio to X-ray light curves in Figure 2. The model fully captures the observed evolution across nine orders of magnitude in frequency and over three orders of magnitude in time.

The bulk Lorentz factor of the ejecta, Γ, can be calculated from a knowledge of the deceleration time and the parameters of the explosion. In the internal-external shock model, we expect the deceleration time to roughly match the duration of the burst. Since the *Swift*/BAT $T_{90} \approx 163$ s and the optical flux is already declining at ≈ 258 s (Melandri et al. 2013) we take $t_{\rm dec} \approx 200$ s. Using the relation $t_{\rm dec} \approx 29(1+z)E_{\rm K,iso,52}\Gamma_{1.5}^{-1}A_*^{-1}$ (Zou et al. 2005), we find $\Gamma \approx 120-150$ at $t_{\rm dec}$, where the range corresponds to the uncertainty in $E_{\rm K,iso,52}$ and A_* due to the uncertainty in $\nu_{\rm a,FS}$. For the median values of $E_{\rm K,iso,52}$ and A_* reported above, we obtain $\Gamma \approx 130$.

In the preceding analysis, we independently determined the RS break frequencies and fit for the parameters of the forward shock. However, the two synchrotron spectra are related since the two shocks propagate in opposite directions from the contact discontinuity. In particular, we expect that at the deceleration time $\nu_{\rm c,RS} \sim \nu_{\rm c,FS}$, $\nu_{\rm m,RS} \sim \nu_{\rm m,FS}/\Gamma^2$, and $F_{\nu,\rm m,RS} \sim \Gamma F_{\nu,\rm m,FS}$. For the parameters given above we find that the FS parameters are $\nu_{\rm c,FS} \approx 8 \times 10^{15}(t_{\rm dec}/200\ {\rm s})^{1/2}$

Hz, $\nu_{\rm m,FS} \approx 2 \times 10^{17} (t_{\rm dec}/200\ {\rm s})^{-3/2}$ Hz, and $F_{\nu,\rm m,FS} \approx 13 (t_{\rm dec}/200\ {\rm s})^{-1/2}$ mJy. For the reverse shock, we have $\nu_{\rm c,RS} \approx 2 \times 10^{16} (t_{\rm dec}/200\ {\rm s})^{-1.3}$ Hz, $\nu_{\rm m,RS} \approx 5.3 \times 10^{17} (t_{\rm dec}/200\ {\rm s})^{-1.3} (\Gamma/130)^{-2}$ Hz, and $F_{\nu,\rm m,RS} \approx 10 (t_{\rm dec}/200\ {\rm s})^{-0.9} (\Gamma/130)^{2}$ mJy, where the power-law indices for $\nu_{\rm c,RS}$, $\nu_{\rm m,RS}$, and $F_{\nu,\rm m,RS}$ are derived from the g-dependent expressions in Zou et al. (2005). We thus confirm that the expected relations between the RS and FS parameters are satisfied to within a factor of two, confirming our basic assumption that the two required emission components indeed correspond to the reverse and forward shocks.

To summarize, a model that includes emission from the reverse and forward shocks consistently explains all available data from radio to X-rays and over a timescale of ~ 200 s to ~ 10 d. The resulting bulk Lorentz factor of the outflow at the deceleration time is $\Gamma \approx 130$.

5. Conclusions

We present a detailed multi-wavelength study of the bright afterglow of GRB 130427A spanning radio to X-rays. From the optical and X-ray data we conclude that the progenitor exploded into a Wind environment, pointing to a massive star. The radio and millimeter observations present a spectrum and temporal evolution that cannot be explained by emission from the forward shock alone. We show that this emission is consistent with synchrotron radiation from a Newtonian reverse shock. With the available multi-band data this is by far the best example to date of reverse shock emission in the radio/millimeter, particularly when compared to previous detections that were based only on only 1–2 epochs at single frequencies (Kulkarni et al. 1999; Berger et al. 2003; Soderberg & Ramirez-Ruiz 2003).

Using multi-wavelength model fitting of the rich afterglow dataset, with the well-sampled light curves spanning over three orders of magnitude in time and nine orders of magnitude in frequency, we determine the properties of the explosion and the circumburst medium. In

particular, we find a low circumburst density, with $A_* \approx 3 \times 10^{-3}$, corresponding to a mass loss rate of $\dot{M} = 3 \times 10^{-8}$ $M_\odot$ yr^{-1} (for a wind velocity of 1,000 km s^{-1}). The low density leads the reverse shock to be in the slow cooling regime ($\nu_{\rm m,RS} < \nu_{\rm c,RS}$), resulting in long-lived radio and millimeter emission. We note that a low density was also inferred for previous GRBs with likely radio reverse shock emission (990123, 020405, and 021211; Chevalier et al. 2004), suggesting that this is a requisite criterion for observable emission from a reverse shock; in a high-density environment, the reverse shock emission will decline rapidly due to efficient cooling of the radiating electrons.

From the derived properties of the explosion and environment we obtain the Lorentz factor of the outflow at the deceleration time, $\Gamma(200\,{\rm s}) \approx 130$, and show that the spectra of the forward and reverse shock at the deceleration time are consistent with theoretical expectations. We infer $E_{\rm K,iso} \approx 7 \times 10^{52}$ erg. However, we note that the forward shock spectrum transitions from fast to slow cooling at ≈ 1200 s, and radiative corrections between this time and $t_{\rm dec} \approx 200$ s are a factor of a few (Sari 1997; Dai & Lu 1998). This suggests that $E_{\rm K,iso} \approx 2 \times 10^{53}$ erg, which is $\approx 20\%$ of the isotropic-equivalent γ-ray energy, implying that the radiative efficiency was large. The lack of an obvious break in the X-ray light curves to ≈ 15 d implies a lower limit of only $\theta_{\rm jet} \gtrsim 2.5^\circ$ on the opening angle of the jet, and hence $E_{\rm K,iso} \gtrsim 2 \times 10^{50}$ erg and $E_{\gamma,{\rm iso}} \gtrsim 10^{51}$ erg. Thus, due primarily to the combination of a large isotropic energy and a low circumburst density, the lack of a jet break at $\lesssim 15$ d is not surprising.

We conclude by noting that GRB 130427A is likely to become the benchmark for reverse shock studies in the JVLA and ALMA era. Our study demonstrates that a complete analysis of the explosion and ejecta properties requires detailed multi-wavelength modeling to leverage the anticipated exquisite data sets.

The Berger GRB group is supported by the National Science Foundation under Grant AST-1107973. CARMA observations were taken as part of the CARMA Key Project, c0999, "A Millimeter View of the Transient Universe" (PI: Zauderer) and VLA observations were taken

as part of programs 13A-046 (PI: Berger), 13A-41 (PI: Corsi), and SE0851 (PI: Cenko). The Karl G. Jansky Very Large Array is operated by the National Radio Astronomy Observatory, a facility of the National Science Foundation operated under cooperative agreement by Associated Universities, Inc. Support for CARMA construction was derived from the states of California, Illinois, and Maryland, the James S. McDonnell Foundation, the Gordon and Betty Moore Foundation, the Kenneth T. and Eileen L. Norris Foundation, the University of Chicago, the Associates of the California Institute of Technology, and the National Science Foundation. Ongoing CARMA development and operations are supported by the National Science Foundation under a cooperative agreement, and by the CARMA partner universities. GMRT is run by the National Centre for Radio Astrophysics of the Tata Institute of Fundamental Research. This work made use of data supplied by the UK Swift Science Data Centre at the University of Leicester.

REFERENCES

Akerlof, C., et al. 1999, Nature, 398, 400

Amati, L., Dichiara, S., Frontera, F., & Guidorzi, C. 2013, GRB Coordinates Network, 14503, 1

Atwood, W. B., et al. 2009, ApJ, 697, 1071

Barthelmy, S. D., et al. 2005, Space Sci. Rev., 120, 143

Barthelmy, S. D., et al. 2013, GRB Coordinates Network, 14470, 1

Berger, E., Soderberg, A. M., Frail, D. A., & Kulkarni, S. R. 2003, ApJ, 587, L5

Bessell, M. S., Castelli, F., & Plez, B. 1998, A&A, 333, 231

Bock, D. C.-J., et al. 2006, in Society of Photo-Optical Instrumentation Engineers (SPIE) Conference Series, Vol. 6267, Society of Photo-Optical Instrumentation Engineers (SPIE) Conference Series

Breeveld, A. A., Landsman, W., Holland, S. T., Roming, P., Kuin, N. P. M., & Page, M. J. 2011, in American Institute of Physics Conference Series, Vol. 1358, American Institute of Physics Conference Series, ed. J. E. McEnery, J. L. Racusin, & N. Gehrels, 373

Burrows, D. N., et al. 2005, Space Sci. Rev., 120, 165

Chevalier, R. A., & Li, Z.-Y. 2000, ApJ, 536, 195

Chevalier, R. A., Li, Z.-Y., & Fransson, C. 2004, ApJ, 606, 369

Corsi, A. 2013, GRB Coordinates Network, 14522, 1

Dai, Z. G., & Lu, T. 1998, MNRAS, 298, 87

Elenin, L., Volnova, A., Savanevych, V., Bryukhovetskiy, A., Molotov, I., & Pozanenko, A. 2013, GRB Coordinates Network, 14450, 1

Evans, P. A., et al. 2009, MNRAS, 397, 1177

Evans, P. A., et al. 2007, A&A, 469, 379

Flores, H., et al. 2013, GRB Coordinates Network, 14491, 1

Foreman-Mackey, D., Hogg, D. W., Lang, D., & Goodman, J. 2012, ArXiv e-prints

Gehrels, N., et al. 2004, ApJ, 611, 1005

Granot, J., & Sari, R. 2002, ApJ, 568, 820

Greisen, E. W. 2003, Information Handling in Astronomy - Historical Vistas, 285, 109

Kalberla, P. M. W., Burton, W. B., Hartmann, D., Arnal, E. M., Bajaja, E., Morras, R., & Pöppel, W. G. L. 2005, A&A, 440, 775

Kennea, J. A., et al. 2013, GRB Coordinates Network, 14485, 1

Kobayashi, S., & Zhang, B. 2003a, ApJ, 597, 455

Kobayashi, S., & Zhang, B. 2003b, ApJ, 582, L75

Kulkarni, S. R., et al. 1999, ApJ, 522, L97

Levan, A. J., Cenko, S. B., Perley, D. A., & Tanvir, N. R. 2013, GRB Coordinates Network, 14455, 1

Margutti, R., et al. 2013, MNRAS, 428, 729

Maselli, A., Beardmore, A. P., Lien, A. Y., Mangano, V., Mountford, C. J., Page, K. L., Palmer, D. M., & Siegel, M. H. 2013, GRB Coordinates Network, 14448, 1

McMullin, J. P., Waters, B., Schiebel, D., Young, W., & Golap, K. 2007, in Astronomical Society of the Pacific Conference Series, Vol. 376, Astronomical Data Analysis Software and Systems XVI, ed. R. A. Shaw, F. Hill, & D. J. Bell, 127

Meegan, C., et al. 2009, ApJ, 702, 791

Melandri, A., Guidorzi, C., Gomboc, A., Japelj, J., & Mundell, C. G. 2013, GRB Coordinates Network, 14452, 1

Morgan, A. N. 2013, GRB Coordinates Network, 14453, 1

Pei, Y. C. 1992, ApJ, 395, 130

Perley, D. A. 2013a, GRB Coordinates Network, 14494, 1

Perley, D. A. 2013b, GRB Coordinates Network, 14451, 1

Perley, R. A., Chandler, C. J., Butler, B. J., & Wrobel, J. M. 2011, ApJ, 739, L1

Roming, P. W. A., et al. 2005, Space Sci. Rev., 120, 95

Sari, R. 1997, ApJ, 489, L37

Sari, R., & Piran, T. 1999a, ApJ, 517, L109

Sari, R., & Piran, T. 1999b, ApJ, 520, 641

Sari, R., Piran, T., & Narayan, R. 1998, ApJ, 497, L17

Sault, R. J., Teuben, P. J., & Wright, M. C. H. 1995, in Astronomical Society of the Pacific Conference Series, Vol. 77, Astronomical Data Analysis Software and Systems IV, ed. R. A. Shaw, H. E. Payne, & J. J. E. Hayes, 433

Soderberg, A. M., & Ramirez-Ruiz, E. 2002, MNRAS, 330, L24

Soderberg, A. M., & Ramirez-Ruiz, E. 2003, MNRAS, 345, 854

Volvach, A., Volvach, L., & Pozanenko, A. 2013, GRB Coordinates Network, 14505, 1

von Kienlin, A. 2013, GRB Coordinates Network, 14473, 1

Woosley, S. E., & Bloom, J. S. 2006, ARA&A, 44, 507

Xu, D., de Ugarte Postigo, A., Schulze, S., Jessen-Hansen, J., Leloudas, G., Kruehler, T., Fynbo, J. P. U., & Jakobsson, P. 2013, GRB Coordinates Network, 14478, 1

Yatsu, Y., et al. 2013, GRB Coordinates Network, 14454, 1

Zauderer, B. A., Berger, E., Chakraborti, S., & Soderberg, A. 2013a, GRB Coordinates Network, 14480, 1

Zauderer, B. A., Berger, E., Chakraborti, S., & Soderberg, A. M. 2013b, GRB Coordinates Network, 14482, 1

Zhu, S., Racusin, J., Kocevski, D., McEnery, J., Longo, F., Chiang, J., & Vianello, G. 2013, GRB Coordinates Network, 14471, 1

Zou, Y. C., Wu, X. F., & Dai, Z. G. 2005, MNRAS, 363, 93

This manuscript was prepared with the AAS LaTeX macros v5.2.

Table 1:: Radio and Millimeter Observations of GRB 130427A

$t-t_0$ (days)	**Observatory**	**Band**	**Frequency** (Hz)	**Flux density** (mJy)	**Uncertainty** (mJy)
0.67	JVLA	C	5.1×10^9	1.5	0.075
0.67	JVLA	C	6.8×10^9	2.5	0.125
2.00	JVLA	C	5.1×10^9	1.82	0.091
2.00	JVLA	C	6.8×10^9	1.76	0.088
2.00	JVLA	K	1.92×10^{10}	1.31	0.0654
2.00	JVLA	K	2.45×10^{10}	1.28	0.0639
2.00	JVLA	Ku	1.35×10^{10}	1.48	0.0741
2.00	JVLA	Ku	1.45×10^{10}	1.42	0.0708
4.70	JVLA	C	5.1×10^9	0.621	0.0311
4.70	JVLA	C	6.8×10^9	0.626	0.0313
4.70	JVLA	Ku	1.35×10^{10}	0.552	0.0276
4.70	JVLA	Ku	1.45×10^{10}	0.527	0.0264
4.70	JVLA	K	1.92×10^{10}	0.469	0.0273
4.70	JVLA	K	2.16×10^{10}	0.508	0.029
9.70	JVLA	C	7.29×10^9	0.416	0.0352
9.70	JVLA	X	8.4×10^9	0.357	0.0434
9.70	JVLA	Ku	1.35×10^{10}	0.37	0.027
9.70	JVLA	Ku	1.45×10^{10}	0.37	0.021
9.70	JVLA	K	1.92×10^{10}	0.38	0.0475
9.70	JVLA	K	2.45×10^{10}	0.43	0.0376

Continued on Next Page…

Table 1 – Continued

$t-t_0$ (days)	**Observatory**	**Band**	**Frequency** (Hz)	**Flux density** (mJy)	**Uncertainty** (mJy)
9.70	JVLA	Ka	3.6×10^{10}	0.427	0.046
3.25	GMRT	L	1.39×10^{9}	0.50	0.10
4.83	GMRT	610	6.1×10^{8}	<0.30	—
5.40	GMRT	610	6.1×10^{8}	<0.26	—
11.6	GMRT	L	1.39×10^{9}	0.45	0.1
0.77	CARMA	3mm	9.25×10^{10}	3.7	0.4
0.81	CARMA	3mm	8.5×10^{10}	3	0.3
1.00	CARMA	3mm	9.25×10^{10}	2.6	0.4
1.84	CARMA	3mm	8.5×10^{10}	0.9	0.25
2.90	CARMA	3mm	8.5×10^{10}	<0.72	—

Table 2: Forward shock parameters for the best fit wind model

Parameter	Value
p	2.23
ϵ_e	$0.30(\nu_{\rm a}/14\ MHz)^{5/6}$
ϵ_b	$0.20(\nu_{\rm a}/14\ MHz)^{-5/2}$
A_*	$3.0\times10^{-3}(\nu_{\rm a}/14\ MHz)^{5/3}$
$E_{\rm K,iso,52}$	$4.9(\nu_{\rm a}/14\ MHz)^{-5/6}$
A_V	0.18 mag
Γ	130
$t_{\rm jet}$	$\gtrsim 15$ days
$\theta_{\rm jet}$	$> 2.5^\circ$
$\nu_{\rm a,FS}$	(12–16)$\times10^6$ Hz
$\nu_{\rm m,FS}$	2.2×10^{13} Hz
$\nu_{\rm c,FS}$	2.8×10^{17} Hz
$\nu_{\rm a,RS}$	5.7×10^{9} GHz
$\nu_{\rm m,RS}$	1.2×10^{10} Hz
$\nu_{\rm c,RS}$	5.9×10^{12} Hz

All frequencies in this table are calculated at Δt = 1 day. The self-absorption frequency of the forward shock at 1 d, $\nu_{\rm a}$, is constrained to 12 MHz $< \nu_{\rm a,7} <$ 16 MHz by the requirement $\epsilon_{\rm e}$, $\epsilon_{\rm b} < 1/3$.

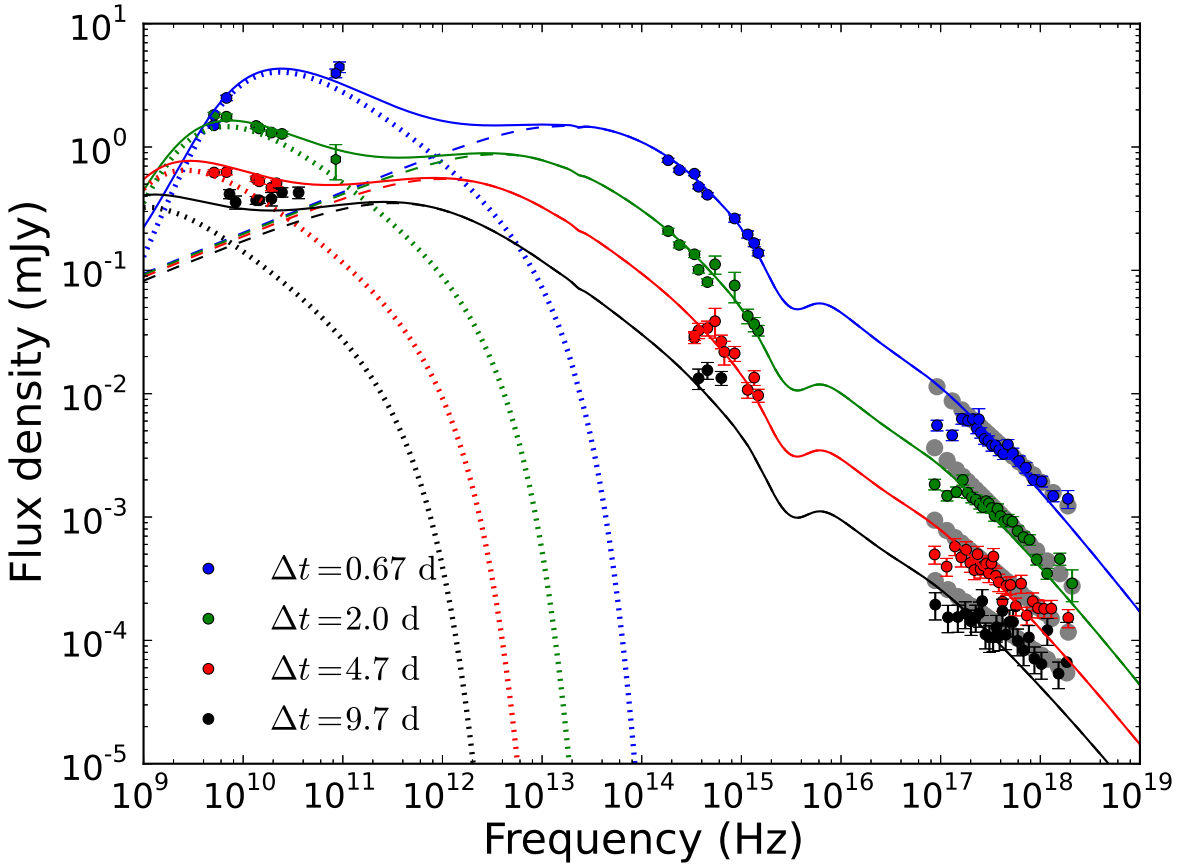

Fig. 1.— The spectral energy distribution of the afterglow at Δt = 0.67, 2.0, 4.7, and 9.7 days. The optical data are small extrapolations from the nearest available data points with a power law of $t^{-1.35}$. The dip in the model around 3×10^{15} Hz is caused by extinction (A_V = 0.18 mag) in the host galaxy. The light grey points represent the unabsorbed models for the X-ray spectra. The dashed and dotted curves show the spectrum of the forward shock and reverse shocks, respectively, while the solid lines are the sum of the two. The combined model fully captures the observed evolution across nine orders of magnitude in frequency.

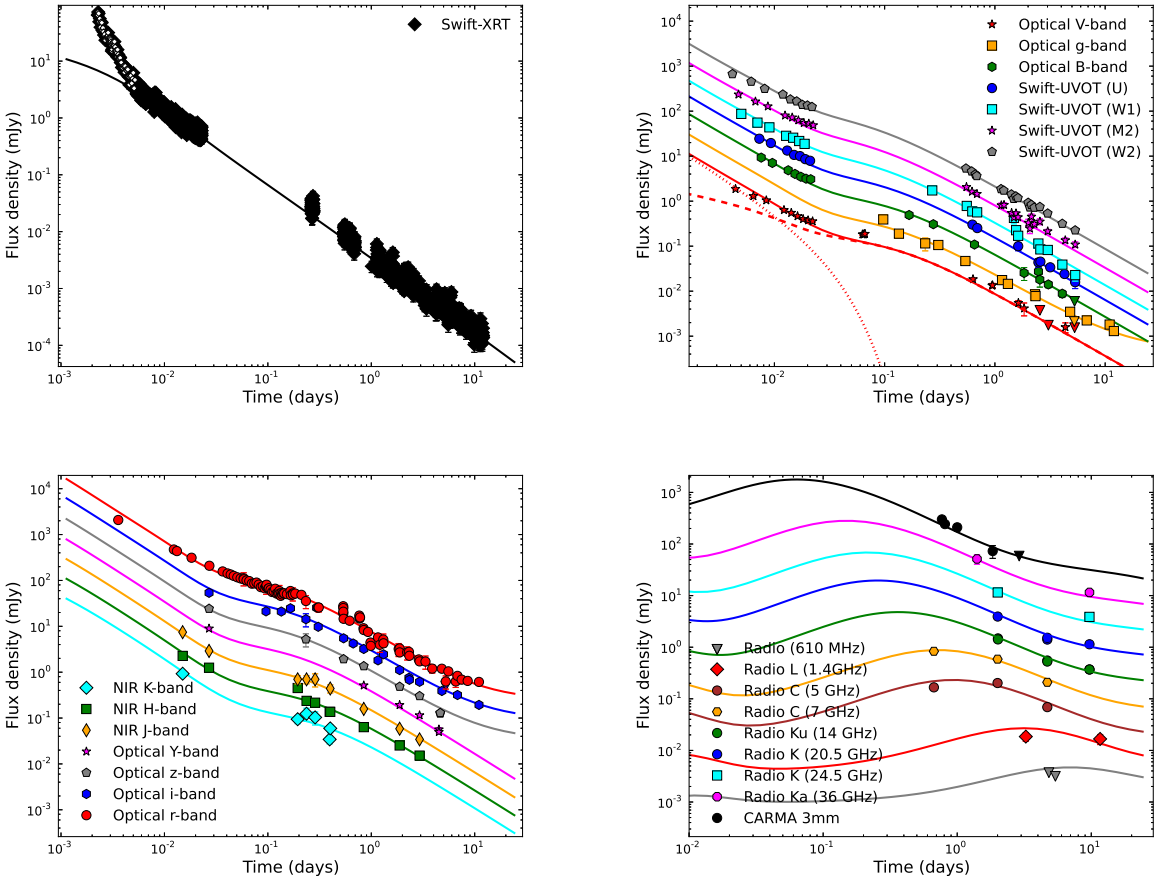

Fig. 2.— Light curves of the afterglow along with the combined reverse shock plus forward shock model (lines). Top left: *Swift*/XRT; top right: *Swift*/UVOT and ground-based *g*-band; bottom left: ground-based *rizYJHK* observations from MMTcam and as reported in GCN circulars; bottom right: GMRT, JVLA and CARMA observations spanning 0.6 to 90 GHz. Adjacent lightcurves have been offset by a factor of 3 for clarity (*U*, *Y*, and the radio Ku band remain on the correct scale). In the top right panel, we show a decomposition of the *V*-band light curve into reverse shock (dotted) and forward shock (dashed) components to guide the reader. The *Swift*/XRT data show a steep-to-shallow transition around Δt = 450 s, which cannot be explained in our model. These data (open symbols) are likely dominated by the low-energy tail of the prompt emission and we exclude them from our fit.